A New Hydrous Iron Oxide Phase Stable at Mid-Mantle Pressures

Huawei Chen[a],*, Sheng-Yi Xie[b], Byeongkwan Ko[a], Taehyun Kim[c], Carole Nisr[a], Vitali Prakapenka[d], Eran Greenberg[d], Dongzhou Zhang[d], Wenli Bi[e], Alp E. Ercan[e], Yongjae Lee[c], and Sang-Heon Shim[a],*

[a]School of Earth and Space Exploration, Arizona State University, Tempe, Arizona, USA; School of Earth Sciences, China University of Geosciences, Wuhan, Hubei, China

[b]School of Physics and Electronics, Hunan University, Changsha, Hunan, China;

[c]Department of Earth System Sciences, Yonsei University, Seoul, South Korea;

[d]GeoSoilEnviroCars, University of Chicago, Chicago, Illinois, USA;

[e]Advanced Photon Source, Argonne National Laboratory, Argonne, IL, USA;

Abstract

The amount of hydrogen stored in the Earth's interior is important for a range of issues, including the volatile incorporation during the Earth formation and the co-evolution of the atmosphere, the hydrosphere, and the interior. Recent experiments found titanium bearing ε-FeOOH in a hydrous basaltic system at 12-19 GPa and 1300 K. Pyrite-type FeOOH was found to be stable at pressures higher than 80 GPa. These discoveries suggest possible hydrogen storage in the mantle transition zone and in the mantle below 1800 km depths, respectively. However, it remains uncertain how the potential deep hydrogen storage can be connected to the shallower storage. Here, we report a new

hydrous iron oxide (η-$Fe_{12}O_{18+x/2}H_x$, $x \approx 2$) stable at pressures between the stability fields of the ε- and the pyrite-type FeOOH. Our experiment also shows that the new η phase can exist together with the major lower mantle minerals including bridgmanite and periclase, making it an important hydrogen-bearing phase in the Earth's deep interior. Because of its limited H_2O storage capacity, which is less than 1/6 of the storage capacity of the pyrite-type phase and the ε phase, the stability of the η phase would result in H_2O loss during water transport in the mid mantle and therefore limit the amount of H_2O potentially stored in the Fe-O-H system of the lower mantle. The large channel in the crystal structure of the η phase could provide potential storage sites for other volatile elements in the deep mantle.

1 Introduction

Hydrogen (H) is the most abundant element in the solar system. However, the amount of H stored in the Earth's interior, which is volumetrically dominant, remains uncertain. Hydrogen can be accommodated in nominally anhydrous minerals. To a depth of 410-km, major mineral phases in the upper mantle may contain a small amount of H, in the form of OH, at 100–500 ppm H_2O (Michael, 1988). Laboratory experiments and diamond inclusion studies have shown that the mantle transition zone between depths of 410 and 660 km may contain much more H as OH in the main mineral phases (wadsleyite and ringwoodite) (Kohlstedt et al., 1996; Pearson et al., 2014) at least locally. The lower

mantle represents 55% of the Earth's volume and therefore the possible storage of H in this region is important to the budget of H in the interior. However, the dominant minerals in the lower mantle, bridgmanite and ferropericlase, seem to have very low H_2O storage capacities (Bolfan-Casanova et al., 2002; Panero et al., 2015).

Hydrous phases would form when nominally anhydrous phases are saturated with hydrogen (Hirschmann, 2006). Although the amounts of possible hydrous phases in the mantle are uncertain, the high concentrations of H in these phases provide possible storage for a significant amount of H in the deep mantle. Two recent experimental studies documented that ε-FeOOH (hereafter ε), containing some Ti, is stable from 12-19 GPa at 1300 K in a hydrous mid-oceanic ridge basaltic (MORB) composition (Liu et al., 2018; Nishihara and Matsukage, 2016; Ono, 1998). Therefore, ε-FeOOH can be important for storage and transport of hydrogen in the upper mantle and the mantle transition zone. At pressures above 80 GPa, the pyrite-type FeOOH phase (hereafter py) is stable. However, the H content in the py phase is still under debate (Liu et al., 2017; Nishi et al., 2017). A series of hydrous phases have been discovered at the lower mantle conditions, most notably $CaCl_2$-type structured phases, such as δ-AlOOH, ε-FeOOH, and H-$MgSiO_2(OH)_2$ (phase H), and pyrite-type structured phases, such as py-FeO_2H_x (x<1) and py-FeOOH (Liu et al., 2017; Nishi et al., 2017, 2014; Sano et al., 2008; Suzuki et al., 2000). These phases appear to form solid solutions with each other in the mantle-related chemical systems (Nishi et al., 2019, 2015; Ohira et al., 2014; Pamato et al., 2015; Yuan et al.,

64 2019). Therefore, it is important to know if the water storage in the shallow mantle can be
65 connected to the potential storage in the deep mantle.
66
67 For Fe-O-H system, far fewer data points – and larger gaps between them – exist at the
68 mid-mantle *P–T* conditions. Therefore, it is unclear if the ε phase (a low-pressure
69 polymorph) transitions directly to the py phase or if an intermediate phase exists between
70 the ε and py phases. This uncertainty raises a question of whether hydrous iron oxide can
71 play a role in the hydrogen (or "water") cycle for a large depth range of the mantle. Here,
72 we report a series of experiments on Fe–O–H systems conducted at the *P–T* conditions of
73 the mid-mantle in the laser-heated diamond-anvil cell (Table 1). We discovered a new
74 hexagonal phase (hereafter η) in the system at 56–83 GPa and high temperatures. Even
75 though it can be formed in a water-saturated system, the η phase contains a much smaller
76 amount of H_2O compared with the ε and py phases.
77
78 # 2 Methods
79
80 ## 2.1 Laser heated diamond anvil cell
81 We loaded pure hematite or goethite (Alfa-Aesar) pre-pressed foil to a symmetric
82 diamond anvil cell (DAC) chamber. Either H_2O or Ne was loaded as a pressure medium.
83 Olivine $(Mg_{0.94}Fe_{0.06})_2SiO_4$ was loaded with H_2O in a separate experiment to examine the
84 stability of hydrous iron oxides in Mg-rich mantle related systems. Detailed information

on experimental runs can be found in Table 1. Diamond anvils with 200 μm culets and 150 μm beveled culets were used for experiments at pressures lower and higher than 65 GPa, respectively. An indented rhenium gasket was drilled for a sample chamber with a 90 or 120 μm in diameter, depending on the cullet size. We loaded a gold particle in the sample chamber for pressure calculation from the measured unit-cell volume (Ye et al., 2017). To prevent potential alloying between Fe and Au at high pressures, the Au grain was separated from the sample foils. We placed a few spacer grains less than 10 μm below and above the sample foil to form layers of pressure medium between the sample and diamond anvils for thermal insulation. The spacer grains were chosen from the starting materials.

Table 1. Experimental runs conducted in this study. We include unit-cell parameters of the observed phases at high pressures and 300 K after laser heating. Temperature uncertainty is approximately 100 K. Other estimated 1σ uncertainties are provided in parentheses. *P*: Pressure, *T*: temperature, S.M.: starting materials, Med.: pressure transmitting medium, Ol: olivine, Hem: hematite, Goe: goethite, η: $Fe_{12}O_{19}H_2$, py: pyrite-type FeOOH, and ε: $CaCl_2$-type FeOOH.

Runs	*P* (GPa)	*T* (K)	S.M.	Med.	η			py	ε
					V (Å^3)	*a* (Å)	*c* (Å)	*V* (Å^3)	*V* (Å^3)
103a	82(4)	1558	Hem	H_2O	221.24(4)	10.01(1)	2.549(1)	88.33(2)	47.7(2)
103b	83(4)	1720	Hem	H_2O	218.12(7)	9.93(3)	2.554(3)	87.79(7)	47.7(1)
204a	51(3)	1420	Hem	H_2O					49.5(1)
204b	85(4)	1880	Hem	H_2O				88.09(6)	47.6(1)
204c	93(5)	2008	Hem	H_2O				87.08(4)	47.2(1)
204d	96(5)	1845	Hem	H_2O				86.94(7)	
301a	96(5)	1675	Hem	H_2O				86.89(7)	47.3(2)
301b	106(5)	2051	Hem	H_2O				86.12(5)	
416	59(4)	1490	Hem	H_2O					49.5 (2)
417a	56(3)	1576	Hem	H_2O	233.51(10)	10.23(5)	2.576(1)		49.6(1)
417b	63(3)	1556	Hem	H_2O	230.82(10)	10.18(4)	2.572(2)		49.2(1)
417c	63(3)	2035	Hem	H_2O	230.82(10)	10.18(4)	2.572(2)		49.2(1)
504	74(4)	1631	Hem	H_2O	224.15(20)	10.07(5)	2.552(2)		47.9(1)
104a	64(3)	1400	Goe	Ne	234.21(15)	10.16(5)	2.624(2)		48.9(1)
104b	61(3)	1943	Goe	Ne	234.21(15)	10.16(5)	2.624(2)		48.9(1)
612	67(3)	1500	Goe	H_2O	233.29(15)	10.14(5)	2.620(2)		
ol18a	99(3)	2160	Ol	H_2O	230.8(15)			85.64(10)	
ol18b	106(3)	2176	Ol	H_2O				85.39(10)	

104 2.2 X-ray diffraction

105

106 We measured X-ray diffraction (XRD) patterns of the sample in the laser-heated DAC at
107 beamline13IDD and 13BMC at the GeoSoilEnviroCARS (GSECARS) sector
108 (Prakapenka et al., 2008; Zhang et al., 2017) of the Advanced Photon Source.
109 Monochromatic X-ray beams with beam sizes of 3×4 μm^2 and 12×18 μm^2 at 13IDD and
110 13BMC, respectively, were focused on the sample. We have collected diffraction data for
111 samples with an X-ray wavelength of 0.4133 or 0.434 Å with a Pilatus detector. For
112 heating, two near-infrared laser beams (1 μm wavelength) were focused on the sample
113 through both sides of DAC with a hot spot size of 20–25 μm^2 at beamline 13IDD. The
114 laser beams were aligned co-axially with the X-ray beam so that we can measure
115 diffraction patterns from the center of the heating spots. Temperatures of the sample were
116 calculated by fitting the thermal radiation spectra to the Planck equation from both sides
117 of the sample. In each run, we heated the samples for at least 10 min. In run 612, to
118 obtain a single phase, we heated the sample for 2 hours. We conducted diffraction pattern
119 measurements both during laser heating and at 300 K before and after laser heating. At
120 high temperatures, we calculated thermal pressures from the thermal expansion factor of
121 ice VII (Fei et al., 1993). Except for heating run 104 which was conducted at Arizona
122 State University, all the heating was conducted at APS. The measured diffraction images
123 (Fig. 1 and S1) were integrated to diffraction patterns in the Dioptas package (Prescher
124 and Prakapenka, 2015). We performed phase identification and peak fitting using a

pseudo-Voigt profile shape function in the PeakPo package (Shim, 2017). The crystal structure was obtained from powder patterns in Endeavour, Fox, and Superflip (Favre-Nicolin and Černỳ, 2002; Palatinus and Chapuis, 2007; Putz et al., 1999). Rietveld refinements were performed with the general structure analysis system (GSAS-II) (Toby and Von Dreele, 2013). We refined phase fractions first, then atomic positions, lattice parameters and spherical harmonic terms for preferred orientation. After reaching a good visual fit, we refined all the parameters together to further reduce residuals after background subtraction, $R_{wp-bknd}$. We achieved $R_{wp-bknd} < 1.8\%$ in all the refinements.

2.3 Synchrotron Mössbauer Spectra of the η phase

For the Mössbauer data, the sample was synthesized from a $Fe_2O_3 + H_2O$ mixture at 62 GPa and 1600 K in LHDAC. In order to enhance the Mössbauer signal, we used ^{57}Fe enriched (67%) Fe_2O_3. X-ray diffraction of the sample indicates that the majority of the sample is the η phase with a small amount of the ε phase. Nuclear forward scattering was conducted at sector 3 of APS. We focused a 14.4-keV X-ray beam on an area of 6×6 μm^2 in the sample. The storage ring was operated in top-up mode with 24 bunches separated by 153 ns. We measured nuclear resonant scattering in a time window of 15–130 ns with a data collection time of 30 min. We measured synchrotron Mössbauer spectra at high pressure after temperature quench (Fig. S2).

146 The fitting was performed for the measured spectrum using the CONUSS package
147 (Sturhahn, 2000). At the beginning of all the spectral fittings, we conducted Monte-Carlo
148 search in CONUSS in order to avoid non-uniqueness of the optimized fitting solutions.
149 Because we detected a small amount of the ε phase from XRD for the sample we used for
150 Mössbauer spectroscopy, we included the Mössbauer parameters of the ε phase obtained
151 from a separate measurement for pure ε phase (to be reported elsewhere). For the isomer
152 shift, we measured a separate spectrum with the sample and a $FeSO_4 \cdot 7H_2O$ standard.
153
154 2.4 First-principles calculations of the η phase
155
156 First-principles calculations were performed within the framework of density functional
157 theory (DFT) (Hohenberg and Kohn, 1964; Kohn and Sham, 1965), as implemented in
158 Vienna Ab initio Simulation Package (VASP) code (Kresse and Furthmüller, 1996).
159 Projector augmented wave (PAW) potentials were used in all the calculations to describe
160 the interactions between core and valence electrons (Blöchl, 1994). Considering the good
161 agreement between the experimental and the simulated lattice parameters in a Fe–O–H
162 system in a previous study (Lu and Chen, 2018), we implemented Perdew-Burke-
163 Ernzerhof (PBE) functional (Perdew et al., 1996) for the exchange-correlation
164 interactions of electrons. Plane-wave basis with a cutoff energy of 500 eV and *k*-point
165 sampling of $2\pi \times 0.025$ Å^{-1} were employed to obtain the precise total energy at 0 K
166 (without zero-point vibration) and 40 to 85 GPa (approximately to experimental

pressures). We relaxed the crystal structure until all the stress forces of atoms were smaller than 0.01 eV/Å.

3 Results

3.1 A new iron oxide phase in Fe-O-H at high pressure-temperature

In our laser-heated diamond-anvil cell (LHDAC) experiments with a hematite starting material in an H_2O medium at 63 GPa and 1556 K, at least nine new diffraction lines were observed whereas the diffraction peaks from hematite disappeared (Fig. 1). Similar diffraction pattern was observed with α-FeOOH in a Ne medium at 64 GPa and 1700 K (Table 1). The new peaks appeared within two minutes of laser heating and grew steadily with heating. After temperature quench, for better coverage toward the lower 2θ angles (i.e., higher *d*-spacings), the laser mirrors were removed from the X-ray beam path, enabling the detection of high *d*-spacing lines up to 9.6 Å. We found a diffraction line at *d*-spacing 8.856 Å. This low angle line was the key when constraining the shape of the unit cell (Fig. 1c). The new lines were not associated with any known polymorphs of Fe_2O_3 (including hematite, post-perovskite, Rh_2O_3-II type phases, and other iron oxide stable at the pressure range) (Bykova et al., 2016), FeH_x (dhcp and fcc), FeOOH (ε and py

186 phases), or H_2O. At the beginning of laser heating, weak ε peaks were observed at 56–83
187 GPa and 1400–1720 K. With further heating, the peaks of the ε phase become weaker
188 while the intensity of the η phase increases at these *P–T* conditions. Therefore, the η
189 phase is likely the high temperature phase of the ε phase at 56-83 GPa.
190
191 The py phase appeared together with the η phases at 83 GPa and 1720 K (also a small
192 amount of the ε phase). Above this pressure, the η phase disappeared and the py phase
193 became dominant, with a small amount of the ε phase in diffraction patterns (Runs 103
194 and 301 in Table 1; Fig. S3). Therefore, the stability field of the η phase is located at a
195 lower pressure than that of the py phase, while likely at a higher pressure than the ε phase
196 (Fig. 2). The Fe–O–H system has been investigated at high *P–T* in recent years (Gleason
197 et al., 2013; Hu et al., 2016; Liu et al., 2017; Nishi et al., 2017). These studies, however,
198 explored mostly pressures where the η phase is unstable. A study reported py-FeO_2H_x at
199 72 GPa and 2300 K (Hu et al., 2017), close to where we begin to observe a transition
200 from the η phase to the py phase (Fig. 2). However, diffraction patterns were not reported
201 for those *P–T* conditions. Another study examined FeOOH, reporting it as the possible ε
202 phase at 59 GPa and 2000 K and 79 GPa and 2100 K (Hu et al., 2016), but X-ray
203 diffraction pattern for the observation was not reported.
204
205

206

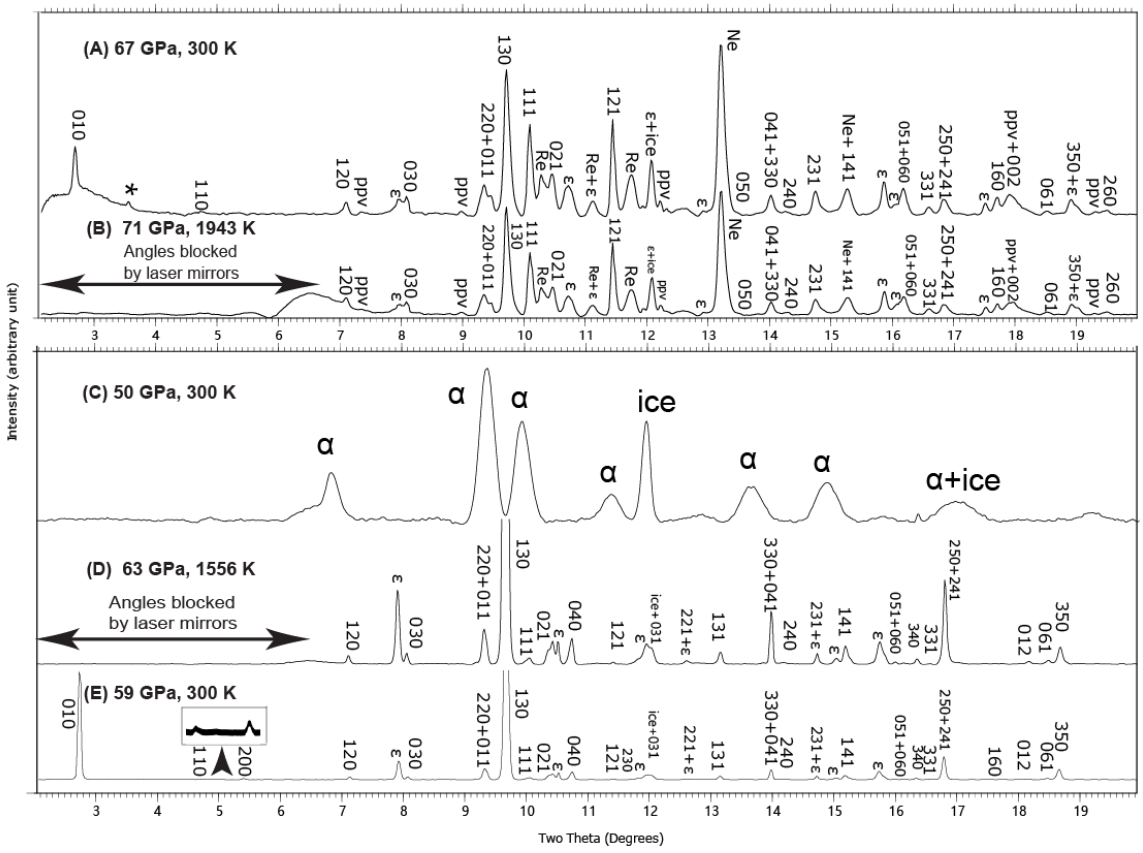

207

208

209 Fig. 1. X-ray diffraction patterns of the new η phase at high P–T. The top panel shows

210 diffraction patterns from an experiment with a goethite starting material in a Ne medium

211 (A) after laser heating and (B) during laser heating at 71 GPa and 1943 K. The bottom

212 panel shows the η phase formed from laser heating of an Fe_2O_3 hematite starting material

213 in an H_2O medium (C) before laser heating, (D) during laser heating at 63 GPa and 1556

214 K, and (E) after laser heating. The inset in (E) shows zoom-in view for 110 and 200

215 peaks. We show the Miller indices for the η phase. The wavelength of the X-ray beam

216 was 0.4133 Å. Phase identification: α: hematite, ε: ε -FeOOH, ppv: Fe_2O_3 ice: ice VII,

217 Ne: Neon pressure medium, and * : unidentified line.

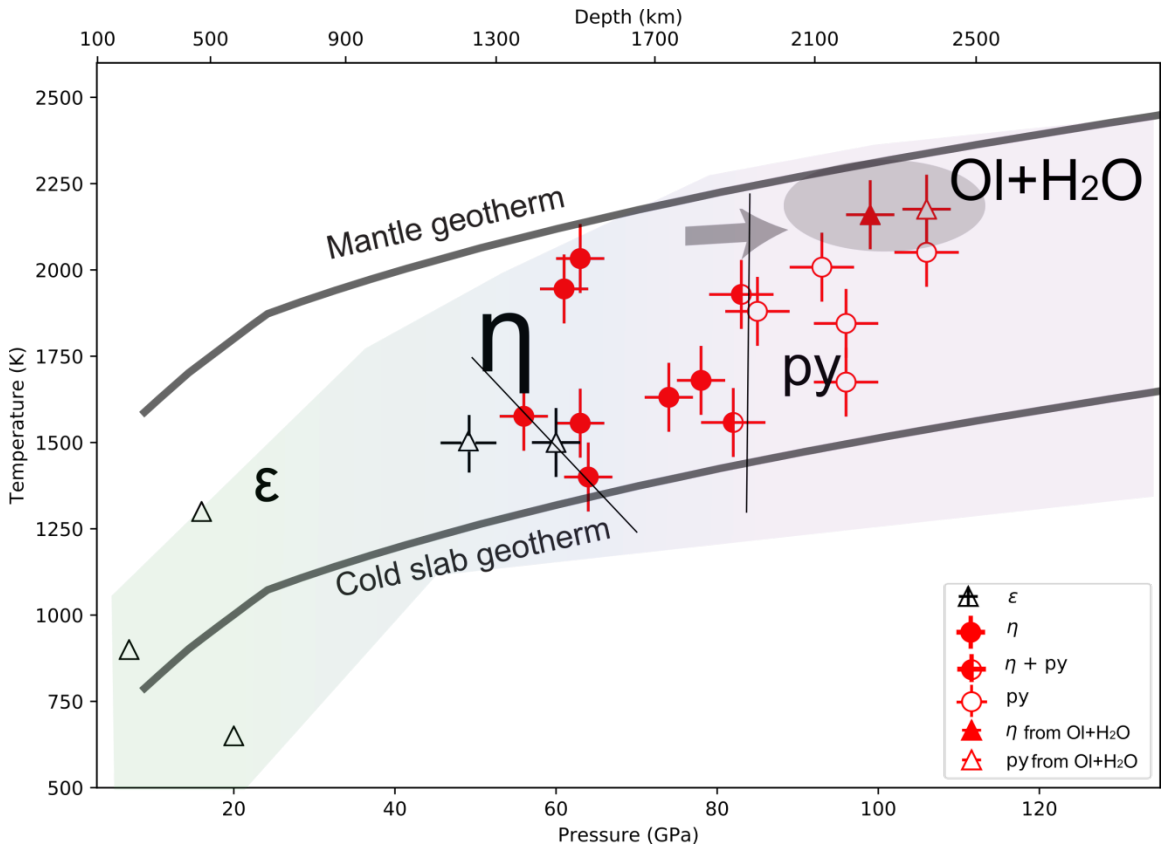

Fig. 2. The pressure-temperature conditions for the phases observed in Fe–O–H and Fe-Mg-Si-O-H systems. The closed and open circles indicate the observations of the η and py phases in our experiments, respectively. The half-filled circles are for observations of the η + py phases in our experiments. The data points from previous studies are shown for the ε phase in open triangles (Dyuzheva et al., 2006; Gleason et al., 2008; Nishi et al., 2017; Nishihara and Matsukage, 2016). The mantle geotherm is from Brown and Shankland (1981). The two thin lines show the conditions where phase changes were observed. The thick gray arrow indicates potential expansion of the *P*-*T* stability of the η phase in Mg-Fe-Si-O-H system.

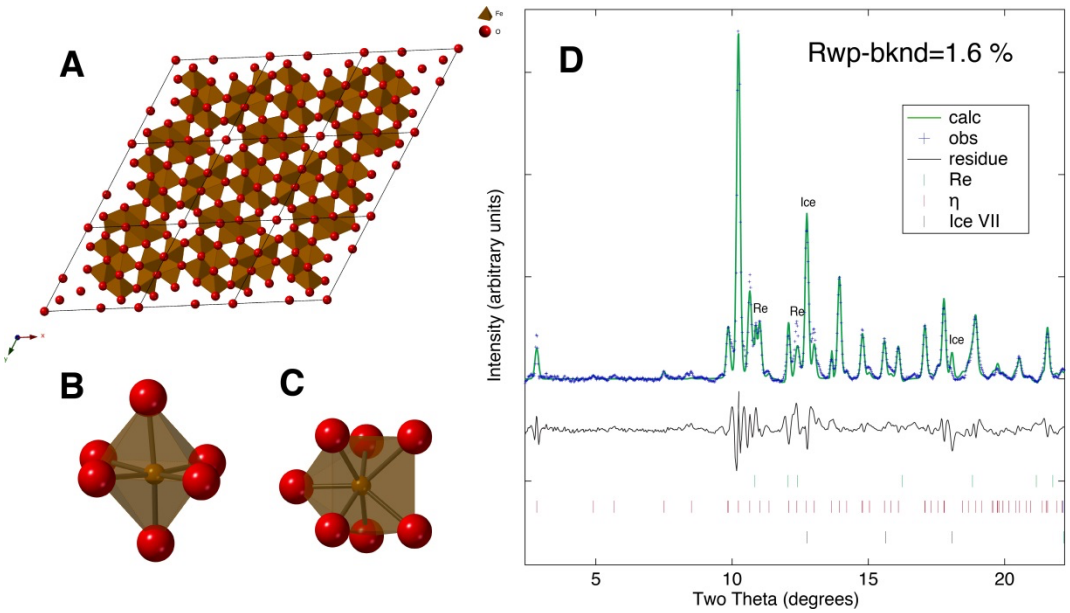

Fig. 3. The crystal structure model for the η phase from Rietveld refinements. (A) The crystal structure of the η phase along the c axis. (B and C) The Fe–O polyhedral with 6 and 7–fold coordination, respectively. (D) The Rietveld refinement for a diffraction pattern measured at 62 GPa and 300 K after laser heating: a = 10.14(1) Å and c = 2.62(1) Å for the η phase, and a = 2.70(1) Å for ice VII. The wavelength of the X-ray beam was 0.434 Å.

238 3.2 Crystal structure of the η phase

239

240 Although first principles and experimental studies have discovered some iron oxide
241 phases at high pressures (Bykova et al., 2016; Weerasinghe et al., 2015), none of the
242 existing structures fit our diffraction patterns. In order to solve the crystal structure of the
243 η phase, we conducted a series of analyses presented in the supplementary information
244 using both powder diffraction patterns and textured diffraction images.

245

246 Briefly,we first explored candidate space groups from the systematic absence of certain
247 diffraction lines, resulting in $P6_3$ and $P6_3/m$. We then conducted simulated annealing and
248 ab initio assisted Monte Carlo method to solve the crystal structure from powder
249 diffraction patterns in the Endeavour and the Fox packages (Favre-Nicolin and Černỳ,
250 2002; Putz et al., 1999). The crystal structure model we obtained in this way was then
251 used as a starting structure model for Rietveld refinements in GSAS-II (Toby and Von
252 Dreele, 2013). The new crystal structure model yielded a 12:19 molar ratio between Fe
253 and O. The crystal structure solution was also confirmed through comparison with the
254 textured diffraction images (Fig. S1 and Table S1).

255

256 The structural model for the η phase has two crystallographic sites for Fe (Fig. 3 and
257 Table S2). One half of Fe is 6-fold coordinated while the other half is 7-fold coordinated

(Fig. 3c). The 7 coordinated Fe has a capped trigonal prism arrangement of six O atoms with an additional O atom (i.e., 6+1 coordinated Fe). Similar coordination of Fe was also found in an Fe-oxide polymorph at 80 GPa (Bykova et al., 2016). The crystal structure had the corner sharing FeO_6 octahedra and the six FeO_6 octahedra formed a hexagonal channel at the [001] edges of the unit cell, similar to the structure documented in a high-pressure polymorph of $CaMg_2Al_6O_{12}$ called the new aluminum phase (NAL) phase (Miura et al., 2000). The FeO_7 polyhedra were connected with the FeO_6 octahedra by sharing the edges while two layers of FeO_7 have face sharing. This type of face sharing is also shown for the Mg sites with a trigonal prism arrangement in the NAL phase (Miura et al., 2000).

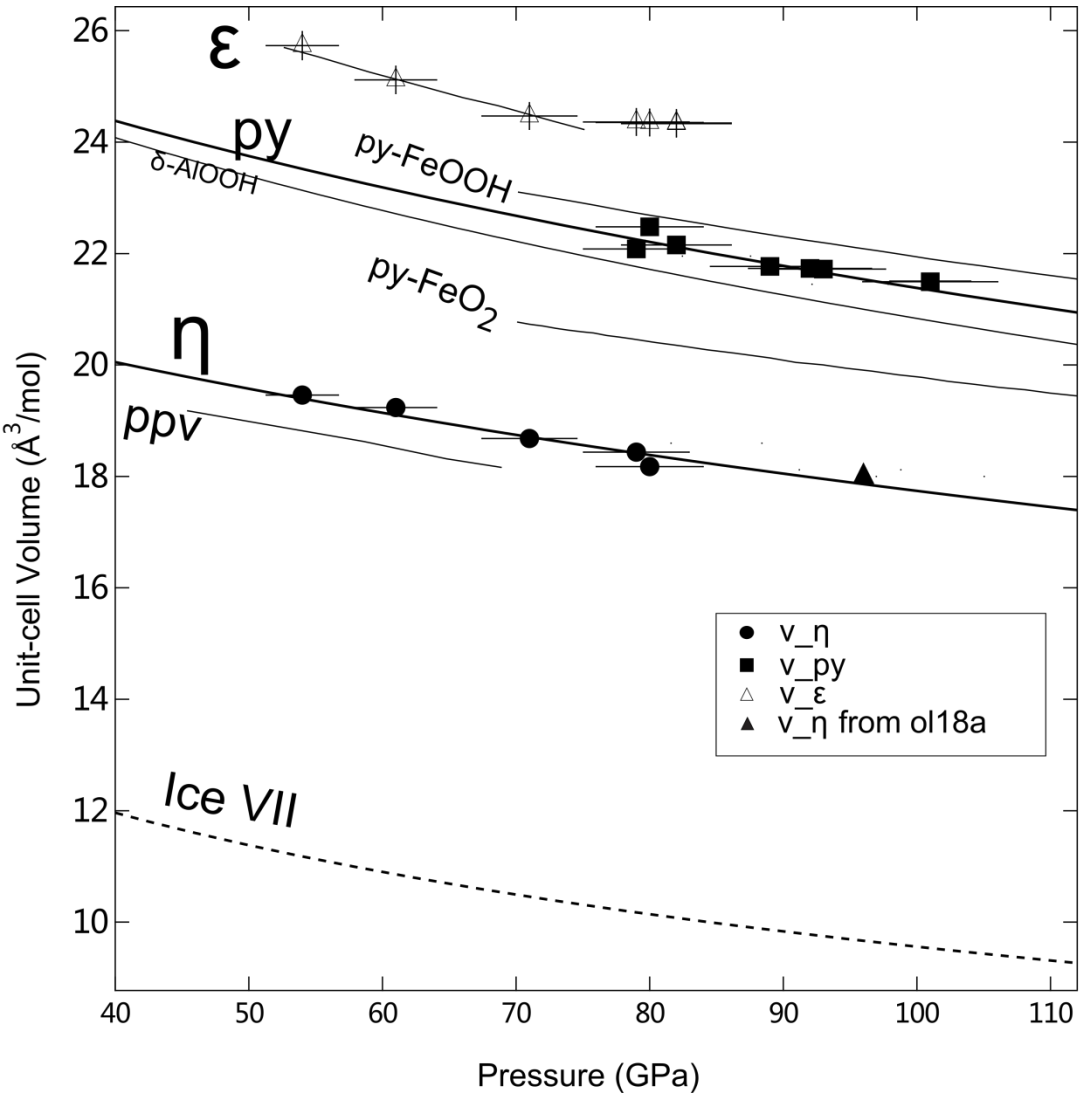

Fig. 4. The unit-cell volume of the η phase at high pressure and 300 K. The unit-cell volumes are normalized by the number of Fe or Al atoms in the unit cells. We also show the unit-cell volumes of the ε and py phases measured in this study. We include the compressional curves of py-FeO_2 (Hu et al., 2017), py (Hu et al., 2017), ε (Gleason et al., 2013), ppv-Fe_2O_3 (Bykova et al., 2013), δ-AlOOH (Mashino et al., 2016) and ice VII

277 (Wolanin et al., 1997) for comparison. The thick lines are calculated values from the

278 equation of state for the py and η phases (see section 3.5 for detail).

279 3.3 Synchrotron Mössbauer Spectra (SMS) of the η phase

280

281 Our Mössbauer measurements for the η phase identified three different Fe sites (Fig. S2
282 and Table S3). Two of the three sites have Mössbauer parameters consistent with low-
283 spin Fe^{3+} with a 1:0.8 ratio between them in fraction. The third site appears to be a high-
284 spin Fe^{3+} site, but its fraction is close to the estimated uncertainty while the other two η
285 sites are more than 10 times greater in fractions and therefore more dominant. The
286 fractions of these two dominant sites and their Mössbauer parameters are consistent with
287 our crystal structure model of the η phase from experimental data in that: (1) there exist
288 largely two Fe sites and the ratio between them is close to 1:1. As we discuss below, we
289 also found that our Mössbauer result is consistent with our first-principles calculations:
290 Fe are likely low-spin Fe^{3+}.

291

292 3.4 Estimation for the hydrogen content in the η phase

293

294 For experiments with starting materials of Fe_2O_3 and H_2O, products of the possible
295 chemical reaction between them should exist on a tie line between these two
296 compositions. The final product should be then:

297

298 $Fe_2O_3 + xH_2O \rightarrow Fe_2O_{3+x}H_{2x}$ (or $Fe_2O_3 \cdot xH_2O$) (1)

299

For example, when $x = 1$, the reaction will produce FeOOH. In contrast, for the laser heating of a goethite starting material in a Ne medium, H_2O exists only in the starting α-FeOOH; therefore, the amount of H_2O is limited. In this experiment, we observed the formation of ice VII as well as the η phase (Fig.1d). The reaction in this experiment can be written as:

$$12\text{FeOOH}\ (\alpha) \rightarrow 5\text{H}_2\text{O}\ (\text{Ice VII}) + \text{Fe}_{12}\text{O}_{19}\text{H}_2\ (\eta) \qquad (2)$$

Although anhydrous ppv-Fe_2O_3 peaks were also observed in some of the diffraction patterns, they were much smaller in intensity compared with other phases and therefore we ignored ppv-Fe_2O_3 in the reaction above. Our measured unit-cell volumes of the ε and pyrite-type phases are consistent with the reported values (Gleason et al., 2013; Nishi et al., 2017) at high pressure and 300 K (Fig. 4). For the py phase, our unit-cell volume values are close to the fully hydrated version of the phase, py-FeOOH. The unit-cell volume of the η phase is smaller than those of both ε and py phases, meaning that less H_2O exists in the η phase than the py phase.

Py-FeOOH is not quenchable at 1 bar (Hu et al., 2017) and therefore is impossible to measure its unit-cell volume and hydrogen content at 1 bar (Chen et al., 2019; Hu et al., 2017). Hu et al. (2017) used the unit-cell volume difference between the dry and hydrated forms of FeO_2 and attributed the difference to the effect of H. We conducted similar

calculations here. For the ε and η phases, no dry form is known, unlike the py phase. Because the ε and η phases can be written in a form of $Fe_2O_3 \cdot xH_2O$, we adapted post-perovskite type (ppv) Fe_2O_3, which is stable form for Fe_2O_3 at this pressures (56-83 GPa), as a dry form (Shim et al., 2009).

The reason we choose ppv-Fe_2O_3 as a dry form to compare is that ppv-Fe_2O_3 has a similar atomic arrangement for the Fe-O bonds. Both ppv-Fe_2O_3 and η phase have two iron positions: one with the FeO_6 octahedral coordination and the other with the FeO_6 trigonal prism coordination (Murakami et al., 2005; Shim et al., 2009). The ratio is 1:1 in both crystal structures. Thus, from crystallographic consideration, the two structures could have a similar unit-cell volume. If anhydrous, however, the η phase should have a smaller unit-cell volume than ppv-Fe_2O_3, because the η phase is stable at higher pressures. However, we observed slightly larger unit-cell volume for the η phase. Thus, the most reasonable explanation is the existence of water in the crystal structure of the η phase but very small amount. The approach has limitations in that the dry forms in Fe_2O_3 and hydrous forms have different crystal structures. Nevertheless, the calculation presented below provides some qualitative insights into the content of H_2O in the η phase.

At 60 GPa, the unit-cell volume of ε is 25.12 $Å^3$ for V/x(Fe) (Fig. 4), which is a unit-cell volume divided by the number of Fe atoms in the unit cell, x(Fe). The value is consistent

341 with the results from Gleason et al. (2013). At the pressure, the post-perovskite type
342 structure (ppv) becames stable in Fe_2O_3, which we take as a dry form. The ppv-Fe_2O_3 has
343 V/x(Fe) = 18.55 Å^3 at 60 GPa. The volume difference between the ε and the ppv-Fe_2O_3
344 can be approximately attributed to the volume occupied by H_2O in the crystal structure of
345 the ε phase. Therefore, we can obtain $\Delta V/x$(Fe) = 6.57 Å^3 for 0.5H_2O.
346
347 The η phase has a larger unit-cell volume than ppv-Fe_2O_3 by $\Delta V/x$(Fe) = 0.62 Å^3 at 60 GPa. Then, we
348 calculated the unit-cell volume for the η phase with one Fe atom to be 19.17 Å^3 at 60 GPa. If the rate of
349 the unit-cell volume change we measured above between the ε phase and ppv-Fe_2O_3 was applicable
350 between the η and ppv phases, we obtain 0.05H_2O for 1 mol of $FeO_{1.5}$. We chose ε-FeOOH as the
351 fully hydrous form to compare the unit-cell volumes because its hydration state and
352 equation of state are better known than those of the py phase.
353
354 For the η phase, we estimated $Fe_{12}O_{18.6}H_{1.2}$ (0.05H_2O per $FeO_{1.5}$) for an ideal composition.
355 The water site in the crystal structure is "Ow" in Table S2. The exact amount of H in the
356 η phase remains uncertain because of the limitations in the methods we used above. The
357 η phase is not quenchable in our experiment, preventing us from conducting further
358 analysis on the amount of H_2O. However, our analysis above strongly suggests that the
359 H_2O content in the η phase should be lower than those in the ε and py phases. The low
360 H_2O content in the η phase can be further supported by our experiments with a goethite

(α-FeOOH) starting material in a Ne medium at 64 GPa and 1900 K (Eq. 2 and Fig. 1d) where we detected formation of H_2O ice by heating.

3.5 The bulk modulus of the η phase

The η phase is not quenchable to 1 bar and therefore we could not obtain unit-cell volume at 1 bar, V_0. Therefore, we fit for V_0 and bulk modulus at 1 bar, K_0, by fixing the pressure derivative of K_0, K_0' to 4. Fitting was conducted for our dataset measured at 56-83 GPa to the Birch-Murnaghan equation of state. We obtained a bulk modulus of 202(15) GPa with a volume projected to 1 bar of 282(2) Å^3. This bulk modulus value is intermediate between those for the ε phase (K_0 = 132 and 162 GPa for high spin and low spin, respectively; Gleason et al., 2013) and pyrite-type phase (K_0 = 220(30) GPa with V_0 = 112(4) Å^3 from this study by fitting data from 79-101 GPa for K_0' = 4).

3.6 First-principles calculations for the η phase

We performed density-functional theory (DFT) calculations for the Fe-O-H system at 40-80 GPa to examine the crystal structure and the enthalpy of the η phase. The crystal structure from the DFT calculations agreed well with the crystal structure model from our experiments even without H_2O: $P6_3/m$ space group with a starting composition $Fe_{12}O_{18}$. However, without H_2O in the crystal structure, the enthalpy of η-$Fe_{12}O_{18}$ was higher than ppv-Fe_2O_3 (Fig. S4), implying that the new η-$Fe_{12}O_{18}$ phase is thermodynamically less

383 stable than ppv-Fe_2O_3. From our experimental results, 0.5–1 mole of H_2O may exist in the
384 η phase. Thus, we relaxed the crystal structure with 0.5 and 1 mole H_2O in the channel.
385
386 After structural optimization, the $P6_3/m$ was retained in the $Fe_{12}O_{18.5}H$ if we ignored the H
387 atom positions. However, when we relaxed the $Fe_{12}O_{19}H_2$, it transformed to a triclinic cell
388 with $\alpha = 89°$, $\beta = 91°$, and $\gamma = 119.1°$. The magnitudes of the a and c parameters of the
389 triclinic cell were in agreement with the hexagonal parent cell as shown in Fig. S4.
390 Overall, the unit-cell volume and the unit-cell parameters observed in our experiments lie
391 in between those of $Fe_{12}O_{18.5}H$ and $Fe_{12}O_{19}H_2$ from the DFT calculations. The similarity in
392 the unit-cell parameters supports our inference on 0.5–1 mole of H_2O in the η phase from
393 our experimental data. The two crystallographic sites of Fe were also confirmed: two
394 sites with six and seven coordination numbers in the low-spin state which is consistent
395 with our Mössbauer data. The O–H bonding at 80 GPa is 0.97 Å, where hydrogen atom
396 lies in between the O–O atoms but asymmetrically in the channel at the four side edges of
397 the unit cell (Fig. 3). The hydrogen atom is located at (0, 0, 0.59) and (0, 0, 0.36) with
398 half occupancy at 80 GPa from the calculations of $Fe_{12}O_{18.5}H$. $Fe_{12}O_{19}H_2$ has a hydrogen
399 position of (0.96, 0.97, 0.18), which is off-centered at 80 GPa. The Fe–O bond distance in
400 FeO_6 is 1.73–1.84 Å from the calculations, which are comparable to the values we
401 obtained from experiments (1.78–1.88 Å) at 80 GPa. The anisotropic Fe–O bond
402 distances are required to form a channel that is also observed in the NAL phase (Miura et
403 al., 2000). The trigonal prism FeO_6 had the Fe–O bonding of 1.93–1.96 Å from the

calculation, while Rietveld refinements yielded 1.90–1.97 Å. The trigonal prism FeO_6 contains another Fe–O bonding with a distance of 2.03 and 2.05 Å in calculations and experimental results, respectively, at 80 GPa. Overall, the Fe–O bond properties from Rietveld refinements agree with the DFT calculations.

The calculated enthalpy of the $Fe_{12}O_{19}H_2$ phase is lower than ppv-Fe_2O_3 + Ice VII, while $Fe_{12}O_{18.5}H$ has a slightly higher energy (e.g., 48 meV/atom) than ppv-Fe_2O_3 + 0.5 Ice VII (Fig. S4 d and e). However, considering high-temperature conditions in our experiments, the thermal energy (e.g. 138 meV/atom at 1600 K) is comparable to the energy difference evaluated at 0 K by DFT. At least, the close energy between the η phase and ppv-Fe_2O_3 + ice VII supports the existence of H_2O in the crystal structure of the η phase and its estimated H_2O content between $Fe_{12}O_{18.5}H$ and $Fe_{12}O_{19}H_2$.

The exact description of strongly correlated electron systems, such as ppv-Fe_2O_3 and the η phase present here, is still challenging in DFT (Meng et al., 2016). Also, the precise total energy calculations through DFT can be limited by the structural uncertainty derived from the varying ratios of H_2O and positions of extra O and H atoms in the η phase. However, our theoretical results generally align with our experimental results (in both lattice parameters and energy differences) and support much lower H_2O content of the η phase than the ε and py phases.

425

426 3.7 Stability of the η phase in the lower mantle chemical system

427

428 In our experiments with an olivine+water starting mixture at 99 GPa and 1700 K, the η
429 phase was formed together with bridgmanite, periclase, and the py phase (Fig. 5). At
430 pressures above 99 GPa, we observed the coexistence of the py phase with bridgmanite
431 and periclase. A recent experiment showed that the py phase can co-exist with
432 bridgmanite and post-perovskite at the conditions of the Earth's deep mantle (Yuan et al.,
433 2019), which is consistent with our result in Ol18b in Table 1. The experimental
434 observation suggests that the η phase can appear in the Mg-rich mantle systems if H_2O is
435 present in the system.

436

437 We also note that Yuan et al. (2019) observed a weak diffraction peak from py-FeOOH in
438 their diffraction patterns. Our py peaks are more intense than the one reported from Yuan
439 et al., (2019) despite the fact that and our starting material contains less Fe (6 mol%)
440 than Yuan et al. (2019). We calculated X-ray diffraction pattern of 94 mol% Brd + 6
441 mol% py-FeOOH (see Fig. S5) using the CrystalMaker and CrystalDiffract software
442 (https://www.degruyter.com/view/journals/zkri/230/9-10/article-p559.xml). The
443 calculation shows that the cubic py-FeOOH has significant intensity even if the
444 concentration is only 6 mol%. The reasons are: (1) Fe had more electrons thus the

445 scattering factor for the py phase is higher, and (2) the diffraction peaks of the cubic py-
446 FeOOH have higher multiplicities than those of orthorhombic Brd.
447
448 There are several possible reasons why Yuan et al., (2019) have low intensity for the
449 peaks of py-FeOOH. First, we used a much larger amount of water that would form more
450 hydrous phases. In contrast, much less water was available in the system of Yuan et al.,
451 (2019), 6-7 wt%. Yuan et al., (2019) observed some Fe remaining in bridgmanite,
452 suggesting that not all the Fe was used for forming FeOOH in their experiments.
453 Secondly, the partitioning of Fe into δ-AlOOH and Brd/ppv undoubtedly affects the
454 amount of FeOOH in the system. Yuan et al. (2019) used 30 mol% Al in the sample
455 which are significantly higher than the pyrolitic composition. We note that ε-FeOOH and
456 δ-AlOOH can form a solid solution (Nishi et al 2019). Thus the formation of δ-AlOOH in
457 Yuan et al. (2019) and therefore possible existence of Fe in the phase would reduce the
458 XRD intensity for py-FeOOH in their experiments. A recent study on a similar chemical
459 system reported that Mg can substitute for Fe in py-$FeOOH_x$ (Hu et al., 2020). The
460 substitution would increase the amount of the py phase, which can result in higher peak
461 intensity of py-FeOOH found in our diffraction patterns compared with Yuan et al.,
462 (2019).
463
464 The pressure where we found the η phase in olivine + water starting material (99 GPa) is
465 higher than the pressure where the phase was observed in Fe-O-H system (<83 GPa). It

can be hypothesized that other elements in the olivine + water experiment may stabilize the η phase to higher pressures. This opens up an intriguing possibility that Mg or Si can dissolve into the η phase.

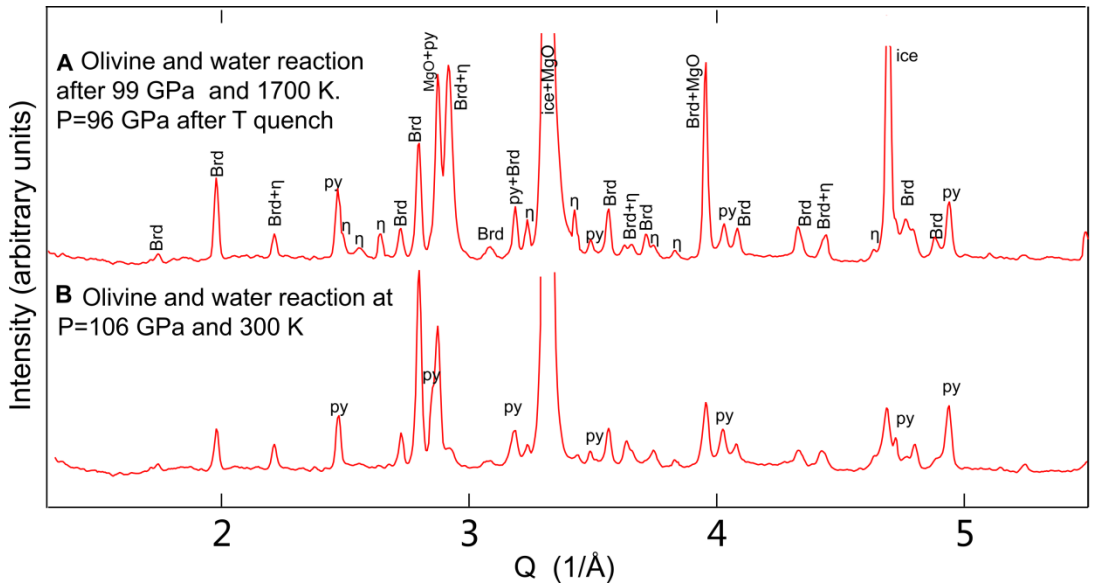

Fig. 5. X-ray diffraction patterns from olivine + H_2O experiments: (A) Brd, Fp, η and py phases at 96 GPa and (B) Brd, Fp, and pyrite phase at 106 GPa in our experiments. In the plot, Q (Q= $2\pi/d$, where d is d-spacing) is used for the x-axis.

4 Implication and Conclusion

The new η phase is stable at the lower pressure side of the py phase stability field while it is stable at higher P–T than the ε phase. The exact amount of H_2O in the new hydrous iron oxide (η phases) remains tentative at 2 wt% at the pressure range 56-83 GPa. However, the unit-cell volume from our experiment and the DFT calculation provide

480 strong indication that the amount of H_2O is lower than those in the ε and py phases,
481 despite its stability under H_2O saturated conditions in our experiments. Because of its
482 lower H_2O storage capacity, the η phase will substantially reduce the amount of H_2O
483 transported deeper into the lowermost mantle in Fe-O-H system, where the py phase
484 would be stable. The potential importance of this new phase for the lower mantle can be
485 further supported by our observation of the coexistence of the η phases together with
486 bridgmanite and ferropericlase in our olivine + H_2O experiments.
487
488 The hydrogen content in the lower mantle is not well constrained. Some amount of
489 hydrogen could be subducted to the deep interior by subducting slabs (Peacock, 1990). If
490 so, the aluminum or iron-rich hydrous phases, for example ε-FeOOH, could play an
491 important role for the transportation of water. The titanium bearing ε-FeOOH was
492 discovered at 12-19 GPa and 1300 K (Liu et al., 2018; Ono, 1998). Thus, MORB can be
493 the water resource for the deep interior even to the depth of the core-mantle boundary if
494 the slabs could be subducted to that depth. However, our result indicates that substantial
495 amount of water would be lost during the phase transition from ε-FeOOH to the η phase.
496
497 The composition of the lithospheric mantle is different from MORB (Griffin et al., 2009).
498 Phase H might form under a hydrous condition after the dehydration of phase D (Nishi et
499 al., 2014). However, phase H has a relative limited stability field ranging from 35 to 60
500 GPa (Ohtani et al., 2014). Aluminum-rich phase H or δ-AlOOH might be the water

carrier for the deep interior instead (Ohira et al., 2014). The lithospheric mantle contain 1-2 wt% Al_2O_3 while the FeO + Fe_2O_3 content in the lithospheric part is about 8 wt% (Griffin et al., 2009). Thus, the discovery of a new hydrous phase in an iron rich system would be important to consider for the subducting lithospheric mantle particularly after the dehydration of phase H. If the water released from phase H is stored in the η phase, the maximum water content at pressures higher than 54 GPa is probably determined by the water storage capacity of the η phase (which is approximately 2 wt%).

The η phase with a novel channeled structure might be worthwhile to consider for variety of volatiles. The NAL phase with a hollandite-type structure is known to be stable at the *P–T* conditions related to the lower mantle (Miura et al., 2000). The NAL phase has three crystallographic sites: one larger site accommodating atoms like Ca and the other two sites accommodating Al or Mg. The channel structure in NAL phase is formed by six AlO_6 octahedra and Ca atoms lie in the channel. The η phase has similar atomic arrangement as the NAL phase, including the channel structure. Our study suggests that the η phase may contain about 2 wt% of water in the channel. While the existence of hydroxyl in the channel of the η phase is likely most logical considering our experimental setup, we cannot rule out the possible existence of other forms of O and H, such as O–O or even H–H, in the channel. The potential existence of these forms is certainly intriguing for the deep mantle geochemistry. Considering that the hollandite-type structure can store some volatiles, such as water and NH_3 (Watenphul et al., 2009; Yang et al., 2017), the η

phase with a channeled structure might also be important for the storage of other volatiles in the deep interior.

ACKNOWLEDGMENTS. This work was supported by NSF grants EAR1321976 and EAR1401270 and a NASA grant (80NSSC18K0353) to S.H.S. H.C. was supported by the Keck Foundation (PI: P. Buseck). Y. L. thanks the Leader Researcher program (NRF-2018R1A3B1052042) of the Korean Ministry of Science and ICT. We thank Kurt Leinenweber and Andrew Chizmeshya for discussions. The results reported herein benefit from collaborations and/or information exchange within NASA's Nexus for Exoplanet System Science (NExSS) research coordination network sponsored by NASA's Science Mission Directorate. The synchrotron experiments were conducted at GSECARS, Advanced Photon Source (APS). GSECARS is supported by NSF-Earth Science (EAR-1128799) and DOE-GeoScience (DE-FG02-94ER14466). APS is supported by DOE, under contracts DE-AC02-06CH11357. The experimental data included in this paper are available by contacting SHDShim@asu.edu or hchen156@asu.edu.

References

Altomare, A., Caliandro, R., Camalli, M., Cuocci, C., Giacovazzo, C., Moliterni, A.G., Rizzi, R., 2004. Automatic structure determination from powder data with EXPO2004. J. Appl. Crystallogr. 37, 1025–1028.

Blöchl, P.E., 1994. Projector augmented-wave method. Phys. Rev. B 50, 17953.

Bolfan-Casanova, N., Mackwell, S., Keppler, H., McCammon, C., Rubie, D.C., 2002. Pressure dependence of H solubility in magnesiowüstite up to 25 GPa: Implications for the storage of water in the Earth's lower mantle. Geophysical Research Letters 29, 89-1-89–4. https://doi.org/10.1029/2001GL014457

Brown, J.M., Shankland, T.J., 1981. Thermodynamic parameters in the Earth as determined from seismic profiles. Geophys J Int 66, 579–596. https://doi.org/10.1111/j.1365-246X.1981.tb04891.x

Bykova, E., Bykov, M., Prakapenka, V., Konôpková, Z., Liermann, H.-P., Dubrovinskaia, N., Dubrovinsky, L., 2013. Novel high pressure monoclinic Fe_2O_3 polymorph revealed by single-crystal synchrotron X-ray diffraction studies. High Pressure Res. 33, 534–545.

Bykova, E., Dubrovinsky, L., Dubrovinskaia, N., Bykov, M., McCammon, C., Ovsyannikov, S., Liermann, H.-P., Kupenko, I., Chumakov, A., Rüffer, R., others, 2016. Structural complexity of simple Fe_2O_3 at high pressures and temperatures. Nat. Commun. 7, 10661.

Chen, H., Shim, S.-H., Leinenweber, K., Prakapenka, V., Meng, Y., Prescher, C., 2018. Crystal structure of $CaSiO_3$ perovskite at 28–62 GPa and 300 K under quasi-hydrostatic stress conditions. Am. Mineral. 103, 462–468.

Chen, H., Zhou, S., Morgan, D., Prakapenka, V., Greenberg, E., Leinenweber, K., Shim, S.-H., 2019. The O–O Bonding and Hydrogen Storage in the Pyrite-type PtO2. Inorganic Chemistry 58, 8300–8307. https://doi.org/10.1021/acs.inorgchem.9b00046

Corma, A., Díaz-Cabañas, M., Jiang, J., Afeworki, M., Dorset, D., Soled, S., Strohmaier, K., 2010. Extra-large pore zeolite (ITQ-40) with the lowest framework density containing double four- and double three-rings. Proc. Natl. Acad. Sci 107, 13997–14002.

Dyuzheva, T., Lityagina, L., Nikolaev, N., Martynov, B., Bendeliani, N., 2006. Growth of single crystals of the high-pressure ϵ-FeOOH phase. Crystallogr. Rep. 51, 342–343.

Favre-Nicolin, V., Černỳ, R., 2002. FOX,free objects for crystallography': a modular approach to ab initio structure determination from powder diffraction. J. Appl. Crystallogr. 35, 734–743.

Fei, Y., Mao, H., Hemley, R.J., 1993. Thermal expansivity, bulk modulus, and melting curve of H2O–ice VII to 20 GPa. J. Chem. Phys. 99, 5369–5373.

Gleason, A., Quiroga, C., Suzuki, A., Pentcheva, R., Mao, W., 2013. Symmetrization driven spin transition in ε-FeOOH at high pressure. Earth Planet. Sci. Lett. 379, 49–55.

Gleason, A.E., Jeanloz, R., Kunz, M., 2008. Pressure-temperature stability studies of FeOOH using X-ray diffraction. Am. Mineral. 93, 1882–1885.

Griffin, W., O'reilly, S.Y., Afonso, J.C., Begg, G., 2009. The composition and evolution of lithospheric mantle: a re-evaluation and its tectonic implications. Journal of Petrology 50, 1185–1204.

579 Hirschmann, M.M., 2006. Water, Melting, and the Deep Earth H2o Cycle. Annual Review of Earth
580 and Planetary Sciences 34, 629–653. https://doi.org/10.1146/annurev.earth.34.031405.125211
581 Hohenberg, P., Kohn, W., 1964. Inhomogeneous electron gas. Phys. Rev. 136, B864.
582 Hu, Q., Kim, D.Y., Liu, J., Meng, Y., Yang, L., Zhang, D., Mao, W.L., Mao, H., 2017.
583 Dehydrogenation of goethite in Earth's deep lower mantle. PNAS 114, 1498–1501.
584 https://doi.org/10.1073/pnas.1620644114
585 Hu, Q., Kim, D.Y., Yang, W., Yang, L., Meng, Y., Zhang, L., Mao, H.-K., 2016. FeO2 and FeOOH
586 under deep lower-mantle conditions and Earth's oxygen–hydrogen cycles. Nature 534, 241–
587 244. https://doi.org/10.1038/nature18018
588 Hu, Q., Liu, J., Chen, J., Yan, B., Meng, Y., Prakapenka, V.B., Mao, W.L., Mao, H., 2020. Mineralogy
589 of the deep lower mantle in the presence of H2O. National Science Review.
590 https://doi.org/10.1093/nsr/nwaa098
591 Images and video generated using CrystalMaker®: a crystal and molecular structures program for
592 Mac and Windows. CrystalMaker Software Ltd, Oxford, England (www.crystalmaker.com),
593 n.d.
594 Kohlstedt, D., Keppler, H., Rubie, D., 1996. Solubility of water in the α, β and γ phases of (Mg,
595 Fe)2SiO4. Contributions to Mineralogy and Petrology 123, 345–357.
596 Kohn, W., Sham, L.J., 1965. Self-consistent equations including exchange and correlation effects.
597 Phys. Rev. 140, A1133.
598 Kresse, G., Furthmüller, J., 1996. Efficient iterative schemes for ab initio total-energy calculations
599 using a plane-wave basis set. Phys. Rev. B 54, 11169–11186.
600 https://doi.org/10.1103/PhysRevB.54.11169
601 Liu, J., Hu, Q., Kim, D.Y., Wu, Z., Wang, W., Xiao, Y., Chow, P., Meng, Y., Prakapenka, V.B., Mao,
602 H.-K., others, 2017. Hydrogen-bearing iron peroxide and the origin of ultralow-velocity
603 zones. Nature 551, 494.
604 Liu, X., Matsukage, K.N., Li, Y., Takahashi, E., Suzuki, T., Xiong, X., 2018. Aqueous fluid
605 connectivity in subducting oceanic crust at the mantle transition zone conditions. Journal of
606 Geophysical Research: Solid Earth 123, 6562–6573.
607 Lu, C., Chen, C., 2018. High-pressure evolution of crystal bonding structures and properties of
608 FeOOH. J. Phys. Chem. Lett. 9, 2181–2185.
609 Mashino, I., Murakami, M., Ohtani, E., 2016. Sound velocities of δ-AlOOH up to core-mantle
610 boundary pressures with implications for the seismic anomalies in the deep mantle. Journal of
611 Geophysical Research: Solid Earth 121, 595–609. https://doi.org/10.1002/2015JB012477
612 Meng, Y., Liu, X.-W., Huo, C.-F., Guo, W.-P., Cao, D.-B., Peng, Q., Dearden, A., Gonze, X., Yang, Y.,
613 Wang, J., others, 2016. When density functional approximations meet iron oxides. J. Chem.
614 Theory Comput. 12, 5132–5144.
615 Michael, P.J., 1988. The concentration, behavior and storage of H2O in the suboceanic upper mantle:
616 Implications for mantle metasomatism. Geochimica et Cosmochimica Acta 52, 555–566.
617 https://doi.org/10.1016/0016-7037(88)90110-X
618 Miura, H., Hamada, Y., Suzuki, T., Akaogi, M., Miyajima, N., Fujino, K., 2000. Crystal structure of
619 CaMg2Al6O12, a new Al-rich high pressure form. Am. Mineral. 85, 1799–1803.

Murakami, M., Hirose, K., Sata, N., Ohishi, Y., 2005. Post-perovskite phase transition and mineral chemistry in the pyrolitic lowermost mantle. Geophys. Res. Lett. 32, L03304. https://doi.org/10.1029/2004GL021956

Nishi, M., Irifune, T., Gréaux, S., Tange, Y., Higo, Y., 2015. Phase transitions of serpentine in the lower mantle. Phys. Earth Planet. Inter. 245, 52–58.

Nishi, M., Irifune, T., Tsuchiya, J., Tange, Y., Nishihara, Y., Fujino, K., Higo, Y., 2014. Stability of hydrous silicate at high pressures and water transport to the deep lower mantle. Nature Geosci 7, 224–227. https://doi.org/10.1038/ngeo2074

Nishi, M., Kuwayama, Y., Tsuchiya, J., Tsuchiya, T., 2017. The pyrite-type high-pressure form of FeOOH. Nature 547, 205–208. https://doi.org/10.1038/nature22823

Nishi, M., Tsuchiya, J., Kuwayama, Y., Arimoto, T., Tange, Y., Higo, Y., Hatakeyama, T., Irifune, T., 2019. Solid Solution and Compression Behavior of Hydroxides in the Lower Mantle. Journal of Geophysical Research: Solid Earth 124, 10231–10239.

Nishihara, Y., Matsukage, K.N., 2016. Iron-titanium oxyhydroxides as water carriers in the Earth's deep mantle. Am. Mineral. 101, 919–927.

Ohira, I., Ohtani, E., Sakai, T., Miyahara, M., Hirao, N., Ohishi, Y., Nishijima, M., 2014. Stability of a hydrous δ-phase, AlOOH–MgSiO2(OH)2, and a mechanism for water transport into the base of lower mantle. Earth and Planetary Science Letters 401, 12–17. https://doi.org/10.1016/j.epsl.2014.05.059

Ohtani, E., Amaike, Y., Kamada, S., Sakamaki, T., Hirao, N., 2014. Stability of hydrous phase H MgSiO4H2 under lower mantle conditions. Geophysical Research Letters 41, 8283–8287. https://doi.org/10.1002/2014GL061690

Ono, S., 1998. Stability limits of hydrous minerals in sediment and mid-ocean ridge basalt compositions: Implications for water transport in subduction zones. Journal of Geophysical Research: Solid Earth 103, 18253–18267.

Palatinus, L., Chapuis, G., 2007. SUPERFLIP–a computer program for the solution of crystal structures by charge flipping in arbitrary dimensions. J. Appl. Crystallogr. 40, 786–790.

Pamato, M.G., Myhill, R., Boffa Ballaran, T., Frost, D.J., Heidelbach, F., Miyajima, N., 2015. Lower-mantle water reservoir implied by the extreme stability of a hydrous aluminosilicate. Nature Geosci 8, 75–79. https://doi.org/10.1038/ngeo2306

Panero, W.R., Pigott, J.S., Reaman, D.M., Kabbes, J.E., Liu, Z., 2015. Dry (Mg,Fe)SiO3 perovskite in the Earth's lower mantle. J. Geophys. Res. Solid Earth 120, 2014JB011397. https://doi.org/10.1002/2014JB011397

Peacock, S.M., 1990. Fluid processes in subduction zones. Science 248, 329–337.

Pearson, D.G., Brenker, F.E., Nestola, F., McNeill, J., Nasdala, L., Hutchison, M.T., Matveev, S., Mather, K., Silversmit, G., Schmitz, S., Vekemans, B., Vincze, L., 2014. Hydrous mantle transition zone indicated by ringwoodite included within diamond. Nature 507, 221–224. https://doi.org/10.1038/nature13080

Perdew, J.P., Burke, K., Ernzerhof, M., 1996. Generalized Gradient Approximation Made Simple. Phys. Rev. Lett. 77, 3865–3868. https://doi.org/10.1103/PhysRevLett.77.3865

Prakapenka, V.B., Kubo, A., Kuznetsov, A., Laskin, A., Shkurikhin, O., Dera, P., Rivers, M.L., Sutton, S.R., 2008. Advanced flat top laser heating system for high pressure research at GSECARS: application to the melting behavior of germanium. High Pressure Research 28, 225–235. https://doi.org/10.1080/08957950802050718

Prescher, C., Prakapenka, V.B., 2015. DIOPTAS: a program for reduction of two-dimensional X-ray diffraction data and data exploration. High Pressure Research 35, 223–230. https://doi.org/10.1080/08957959.2015.1059835

Putz, H., Schön, J., Jansen, M., 1999. Combined method for ab initio structure solution from powder diffraction data. J. Appl. Crystallogr. 32, 864–870.

Ross, N.L., Hazen, R.M., 1990. High-pressure crystal chemistry of $MgSiO_3$ perovskite. Physics and Chemistry of Minerals 17, 228–237.

Sano, A., Ohtani, E., Kondo, T., Hirao, N., Kikegawa, T., 2008. Aluminous hydrous mineral δ-AlOOH as a carrier of hydrogen into the core-mantle boundary. Geophysical Research Letters 35, 3303.

Shim, S.-H., 2017. PeakPo - A python software for X-ray diffraction analysis at high pressure and high temperature. https://doi.org/10.5281/zenodo.810200

Shim, S.-H., Bengtson, A., Morgan, D., Sturhahn, W., Catalli, K., Zhao, J., Lerche, M., Prakapenka, V., 2009. Electronic and magnetic structures of the postperovskite-type Fe_2O_3 and implications for planetary magnetic records and deep interiors. Proc. Natl. Acad. Sci. 106, 5508–5512.

Sturhahn, W., 2000. CONUSS and PHOENIX: Evaluation of nuclear resonant scattering data. Hyperfine Interactions 125, 149–172.

Suzuki, A., Ohtani, E., Kamada, T., 2000. A new hydrous phase delta-AlOOH synthesized at 21 GPa and 1000 C. Physics & Chemistry of Minerals 27, 689–693.

Toby, B.H., Von Dreele, R.B., 2013. GSAS-II: the genesis of a modern open-source all purpose crystallography software package. J Appl Cryst 46, 544–549. https://doi.org/10.1107/S0021889813003531

Watenphul, A., Wunder, B., Heinrich, W., 2009. High-pressure ammonium-bearing silicates: Implications for nitrogen and hydrogen storage in the Earth's mantle. American Mineralogist 94, 283–292.

Weerasinghe, G.L., Pickard, C.J., Needs, R., 2015. Computational searches for iron oxides at high pressures. J. Phys.: Condens. Matter 27, 455501.

Wolanin, E., Pruzan, P., Chervin, J., Canny, B., Gauthier, M., Häusermann, D., Hanfland, M., 1997. Equation of state of ice VII up to 106 GPa. Phys. Rev. B 56, 5781.

Yang, Z., Ford, D.C., Park, J.S., Ren, Y., Kim, S., Kim, H., Fister, T.T., Chan, M.K., Thackeray, M.M., 2017. Probing the Release and Uptake of Water in α-MnO2· x H2O. Chemistry of Materials 29, 1507–1517.

Ye, Y., Prakapenka, V., Meng, Y., Shim, S.-H., 2017. Inter-comparison of the Gold, Platinum, and MgO Pressure Scales up to 140 GPa and 2,500 K. J. Geophys. Res. Solid Earth 2016JB013811. https://doi.org/10.1002/2016JB013811

Yuan, H., Zhang, L., Ohtani, E., Meng, Y., Greenberg, E., Prakapenka, V.B., 2019. Stability of Fe-bearing hydrous phases and element partitioning in the system MgO–Al2O3–Fe2O3–SiO2–H2O in Earth's lowermost mantle. Earth and Planetary Science Letters 524, 115714.

Zhang, D., Dera, P.K., Eng, P.J., Stubbs, J.E., Zhang, J.S., Prakapenka, V.B., Rivers, M.L., 2017. High pressure single crystal diffraction at PX^ 2. JoVE (Journal of Visualized Experiments) e54660.

Supplementary information for: A New Hydrous Iron Oxide Phase Stable in Hydrous Lower-Mantle Systems

Huawei Chen[a],*, Sheng-Yi Xie[b], Byeongkwan Ko[a], Taehyun Kim[c], Carole Nisr[a], Vitali Prakapenka[d], Eran Greenberg[d], Dongzhou Zhang[d], Wenli Bi[e], Alp E. Ercan[e], Yongjae Lee[c], and Sang-Heon Shim[a],*

[a]School of Earth and Space Exploration, Arizona State University, Tempe, Arizona, USA;

[b]School of Physics and Electronics, Hunan University, Changsha, Hunan, China;

[c]Department of Earth System Sciences, Yonsei University, Seoul, South Korea;

[d]GeoSoilEnviroCars, University of Chicago, Chicago, Illinois, USA;

[e]Advanced Photon Source, Argonne National Laboratory, Argonne, IL, USA;

721 **Crystal structure of the new hydrous iron oxide phase**

722

723 We present here details on determining the crystal structure of the η phase. A
724 primitive hexagonal unit cell matches all the observed new peaks well. For example,
725 for the diffraction patterns measured after laser heating at 59 GPa, we observed a peak
726 at 8.85 Å (the lowest angle diffraction line), which provides an important constraint
727 on the *a* axis. Based on the indexing, we obtained the *a* axis of the new structure to be
728 10.227 Å. All the diffraction lines observed at low 2θ angles of 2.5–7.1° can be well
729 indexed with Miller indices of *hk*0 from the *a* parameter. This fitting result indicates
730 that the *c* axis needed to be much smaller in length. We chose lines that cannot be
731 indexed as *hk*0 in search for the *c* axis cell parameter. For example, a line with a *d*-
732 spacing of 2.51 Å cannot be indexed with *hk*0. Among the many attempts we made,
733 the most satisfactory results were found when a line at 2.51 Å is assigned to 011.
734 From this unit cell assignment (a = 10.227(5) Å and c = 2.576(1) Å at 59 GPa and
735 300 K), we can index all the diffraction lines between 2.5°2θ and 25°2θ (or a *d*-
736 spacing range between 9.4 and 0.95 Å). Our Miller index assignment was then tested
737 with EXPO2004 (Altomare et al., 2004), which confirmed the *a* and *c* axis.

738

739 The systematic absence of lines with 00*l* for $l = 2n + 1$ indicates a 6_3 screw axis in the
740 crystal structure of the new η phase. Thus, the space group of the new structure can be

741 $P6_3$ (173), $P6_3/m$ (176), or $P6_322$(182). The three space groups can be distinguished
742 by Laue symmetry 6/*m* or 6/*mmm*, which we discuss below.
743
744 To obtain a pure sample for the η phase, we heated a sample in DAC for an extended
745 period of time at a temperature between 1300–1500 K and 66 GPa. The attempt was
746 successful after 2 hours of laser heating. In the diffraction patterns, only the η phase
747 existed together with ice VII (medium) and weak Re peaks (gasket) as shown in Fig.
748 2d. There are only three diffraction peaks from Re and ice VII with detectable
749 intensities. We oscillated the DAC around the X-ray beam by ±23° during diffraction
750 measurements. Such an operation could enhance random orientation for crystals
751 during diffraction measurements.
752
753 For this diffraction pattern, we used simulated annealing and ab initio assisted Monte
754 Carlo method to solve the crystal structure from powder diffraction in Endeavour and
755 Fox (Favre-Nicolin and Černỳ, 2002; Putz et al., 1999). Two separate methods
756 yielded the same result for crystal structure (Fig. 3) with a composition of $Fe_{12}O_{18}$ in a
757 space group of either $P6_3$ or $P6_3/m$. We could not achieve a reasonable crystal
758 structure with $P6_322$, which we will discuss below using Laue symmetry. When the
759 $P6_3$ space group was used as a starting point, the final structure solution would end up
760 with the $P6_3/m$ space group. Thus, the space group can be assigned as $P6_3/m$. A
761 charge flipping method was also tested, which could not resolve the crystal structure

762 but correctly resolved the 12 Fe atoms (Palatinus and Chapuis, 2007). The charge
763 flipping method requires high-quality diffraction patterns without preferred
764 orientation, which might be the reason for not resolving the structure. Some degree of
765 preferred orientation may still exist despite the effort of oscillating the DAC.
766 Comparison of the obtained unit-cell volume of the η phase with the py phase (or
767 $Fe_{12}O_{24}H_{12}$) shows that the number of O atom should be smaller than 24 (Fig. 4).
768 Otherwise, the density of the lower-pressure phase η becomes higher than that of the
769 py phase.
770
771 We conducted Rietveld refinements in order to obtain the atomic positions of Fe and O
772 atoms (Table S2). A composition $Fe_{12}O_{19}$ was achieved from fitting the powdered
773 pattern. Based on the electron density map in Rietveld refinement, we found another
774 oxygen position in the tunnel in the crystal structure. This oxygen atom is likely to be
775 hydrated because it is unlikely to have a single oxygen atom in the tunnel. The
776 stoichiometry ($Fe_{12}O_{19}$) of this phase also needs two more hydrogens to balance the
777 extra negative charge. Thus, we noted this oxygen atom as Ow in Table S2. The
778 justification for the H_2O content will be discussed below.
779
780 The unit-cell shape of the η phase has a flat shape with much larger *a* axes than the *c*
781 axis. The preferred orientation can be particularly strong depending on the
782 morphology of crystals and pressure transmitting medium (Chen et al., 2018). To

783 obtain a multi-grain type sample, we prepared a separate sample with a small
784 thickness (1μm thick) (run 103). The patterns obtained from this experiment suggest
785 that the sample consisted of a few single crystals of the η phase with their *c* axis
786 aligned parallel to the loading axis of the DAC and incident X-ray beam. In our 2D
787 diffraction images, the well-crystallized η phase produced spotty Debye diffraction
788 rings (Fig. S1). In particular, for the rings at lower angles, we found six main
789 diffraction spots separated from each other by 60 degrees. For example, the ring at
790 8.66 Å of *d*-spacing formed a hexagonal shape. The intensities of the six diffraction
791 spots were nearly the same, confirming the hexagonal crystal structure of the η phase.
792 For the Laue symmetry, the difference between 6/*m* and 6/*mmm* lies in the intensity
793 distribution that is overlapped; thus, it is not possible to distinguish in powder
794 diffraction. For example, the intensities of 210 or 120 spots should be different in 6/*m*
795 but the same in 6/*mmm*. We could take advantage of the textured diffraction patterns
796 to confirm the space group and crystal structure solution. The diffraction spots and
797 corresponding intensities from this textured sample are shown in Table S1 and Fig.
798 S1. The existence of two groups of intensity distributions of the 130 and 310 peaks
799 confirm the 6/*m* Laue symmetry. Thus, the space group can be assigned to $P6_3/m$.
800

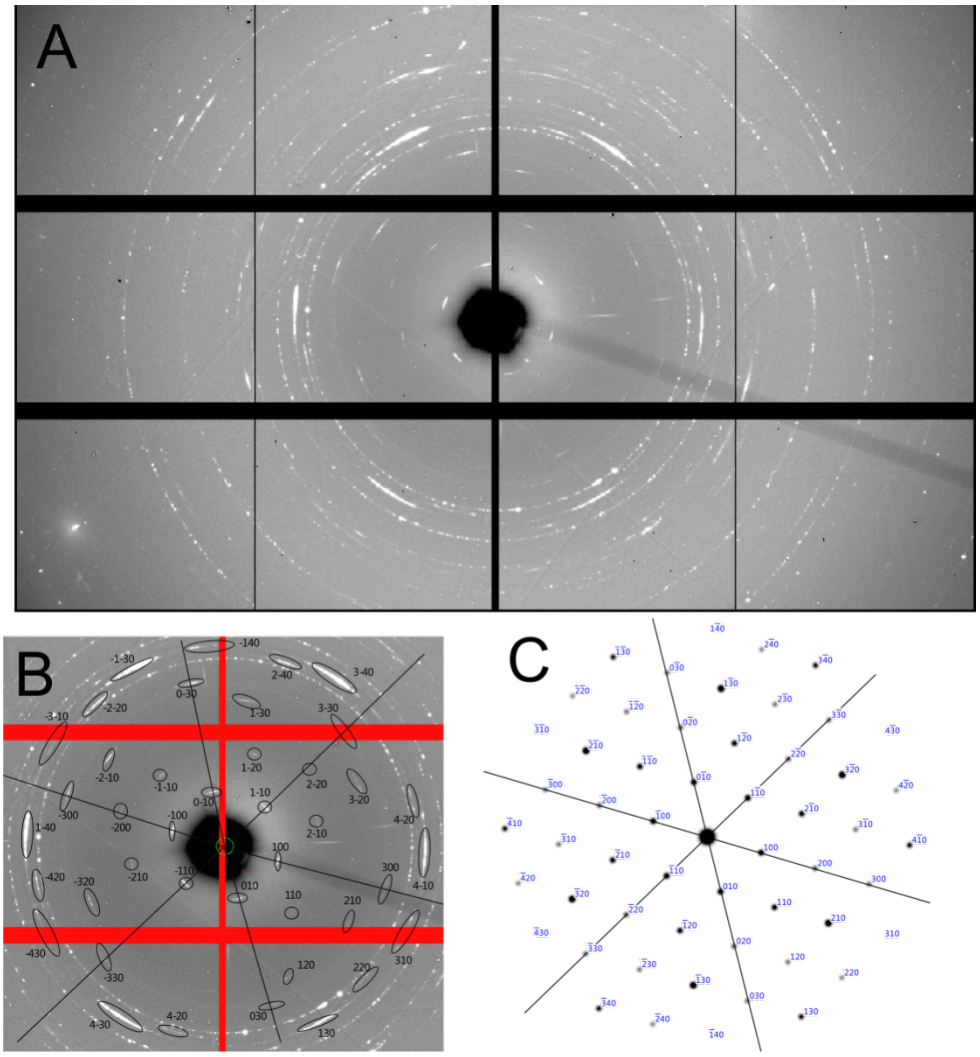

Fig. S1 X-ray diffraction images of the textured η phase sample at 80 GPa: (A) diffraction image from run 103a, (B) diffraction image from run 103a with the Miller indices assigned to the diffraction spots, and (C) calculated single crystal diffraction image for the η phase with the c axis parallel to the loading axis of the DAC and the incident X-ray beam direction. In (B), the green circle at the center indicates the X-ray beam center and the red areas are the gap spaces in the Pilatus 1M CdTe detector. The

809 thin black lines in (B) and (C) are guides for eyes to compare the diffraction spots

810 between experiment and calculation.

811

812 The single crystal diffraction spot positions and intensities were calculated with a
813 12:19 ratio for Fe:O in Table S1 with the *c* axis parallel to the X-ray beam. We then
814 compared the calculation with our textured X-ray diffraction patterns. The intensity
815 partition of overlapped diffraction peaks matched well with the calculation, supporting
816 the crystal structure solution. The textured diffraction pattern showed 37 individual
817 diffraction spots. The crystal structure solution or atomic position will affect every
818 diffraction spot and intensity. The averaged diffraction intensity for the equivalent
819 diffraction spot in the 6/*m* Laue symmetry confirmed the crystal structure solution.
820 The *c* axis of crystals is not exactly parallel to the beam, which can cause some
821 directions to have lower intensities. For example, the 010 direction shows a lower
822 intensity than other directions (Fig. S1). To be able to resolve a crystal structure,
823 coverage of large *d*-spacing is needed in single crystal diffraction. However, the
824 aperture of the used DAC limits the angular coverage to a maximum of 35°2θ. A
825 multi-grain type diffraction can be affected by overlapping of diffraction spots from
826 twined or polycrystals, making it difficult to extract intensity from diffraction spots.
827 The powder diffraction method has successfully solved crystal structures up to 7562
828 Å^3 with 234 atoms (Corma et al., 2010). It is often very difficult to obtain single
829 crystal of sufficient quality for crystal structure determination at high pressure. In
830 addition, for the phases that are only stable at high pressure, such as the η phase in
831 this study, the *d*-spacing information is limited because of the DAC geometry. In this
832 study, we demonstrated that a combination of powder diffraction and textured

833 diffraction can be a powerful method to obtain the crystal structure of such high-
834 pressure phases.
835
836

Table S1. Selected diffraction intensities and angles from textured diffraction patterns. We observed weaker intensities for the spots along the [010] direction due to the slightly misoriented crystal. They are noted with "w". ϕ is the azimuthal angle of the diffraction spot. I_{ave} is a fractional intensity obtained by averaging the intensities of the equivalent diffraction spots. The reference intensity was obtained from the 130 line. I_{calc} is calculated from the crystal structure of $Fe_{12}O_{19}H_2$.

h	*k*	*l*	2θ (◦)	ϕ (◦)	Intensity	Note	*Iavg*	*Icalc*
1	0	0	2.739	155.00	787.4		0.05	0.03
0	1	0	2.739	95.00	205.3	w		
-1	1	0	2.745	35.00	749.6			
-1	0	0	2.739	-25.00	919.3			
0	-1	0	2.740	-85.00	400.0			
1	-1	0	2.745	-145.00	956.6			
1	1	0	4.772	127.00	101.6		0.01	0.02
-2	1	0	4.780	7.00	128.0			
2	-1	0	4.771	-173.00	91.0			
-2	0	0	5.487	-85.00	63.2		0.01	0.01
2	-2	0	5.489	-145.00	113.3			
2	1	0	7.253	138.00	216.9	w	0.04	0.11
3	-2	0	7.265	18.00	346.0			
-2	-1	0	7.267	-42.00	416.2			
1	-3	0	7.255	-102.00	330.5			
3	-2	0	7.259	-162.00	314.4			
1	2	0	7.255	108.00	106.1		0.01	0.01
3	0	0	8.231	155.00	245.16		0.03	0.02
0	3	0	8.233	95.00	100.5	w		
-3	3	0	8.247	35.00	310.4			
-3	0	0	8.231	-25.00	300.8			
0	-3	0	8.237	-85.00	180.2			
3	-3	0	8.244	-145.00	230.2			
2	2	0	9.497	127.00	148.1	w	0.03	0.04
4	-2	0	9.517	67.00	337.7			
-4	2	0	9.489	7.00	227.0			
-2	-2	0	9.486	-53.00	685.1			
2	-4	0	9.497	-113.00	684.7			
4	-2	0	9.482	-173.00	66.0	w		
1	3	0	9.906	170.00	5567.1	w	1.00	1.00
4	-3	0	9.899	110.00	16156.8			
1	-4	0	9.912	50.00	15531.5			
-1	-3	0	9.896	-10.00	8976.0			
3	-4	0	9.897	-70.00	9652.0			
4	-1	0	9.907	-130.00	12211.5			
3	1	0	9.902	80.00	140.0		0.01	0.01
1	-4	0	9.891	-100.00	121.0			

Table S2. The crystal structure of the η phase from Rietveld refinements of a pattern measured at 66 GPa and 300 K. The unit cell parameters are: a = 10.14(5) Å and c = 2.62(2) Å. The space group is $P6_3/m$.

Atoms	x	y	z	Occupancy
Fe1	0.384(2)	0.552(4)	0.25	1
Fe2	0.942(1)	0.694(2)	0.25	1
O1	0.393(3)	0.407(3)	0.75	1
O2	0.883(5)	0.781(2)	0.75	1
O3	0.492(1)	0.720(4)	0.75	1
Ow	0.0	0.0	0.0	0.5(1)

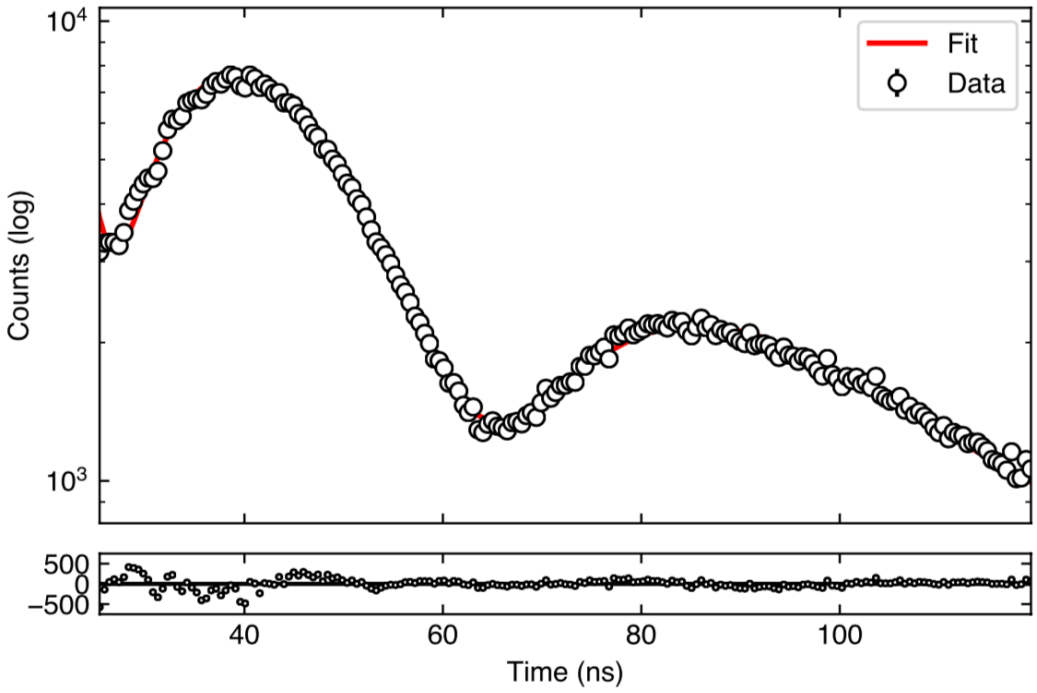

Fig. S2. Synchrotron Mössbauer spectrum of the η phase. The sample was synthesized at 62 GPa and 1600 K (circles, measured intensities; curves, fitted spectra). We show the fit residue at the bottom part of the figure.

Tab. S3. Fitting results for the Mössbauer spectrum of the η phase. We obtain a χ^2 of 4.3 for the fitting; *Wt*: fraction of the site; *IS*: isomer shift (mm/s) with respect to that of $FeSO_4 \cdot 7H_2O$ at 1 bar; *QS*: quadruple splitting (mm/s). The numbers in parentheses are the 1σ estimated uncertainties. A small amount of the ε phase was detected in diffraction pattern. Therefore, we subtracted the effects of the ε phase by fitting the fraction of the phase while we fix other parameters of the ε phase (*Wt* = 0.01, *IS* = 0.15 mm/s, *QS* = 1.34 mm/s for site 1; *Wt* = 0.03, *IS* = 0.78 mm/s; *QS* = 0.08 mm/s; manuscript in preparation).

	site 1	site 2	site 3
Wt	0.53(2)	0.39(2)	0.03(2)
IS (mm/s)	0.11(5)	-0.13(5)	-0.51(5)
QS (mm/s)	1.80(3)	0.79(3)	0.17(3)

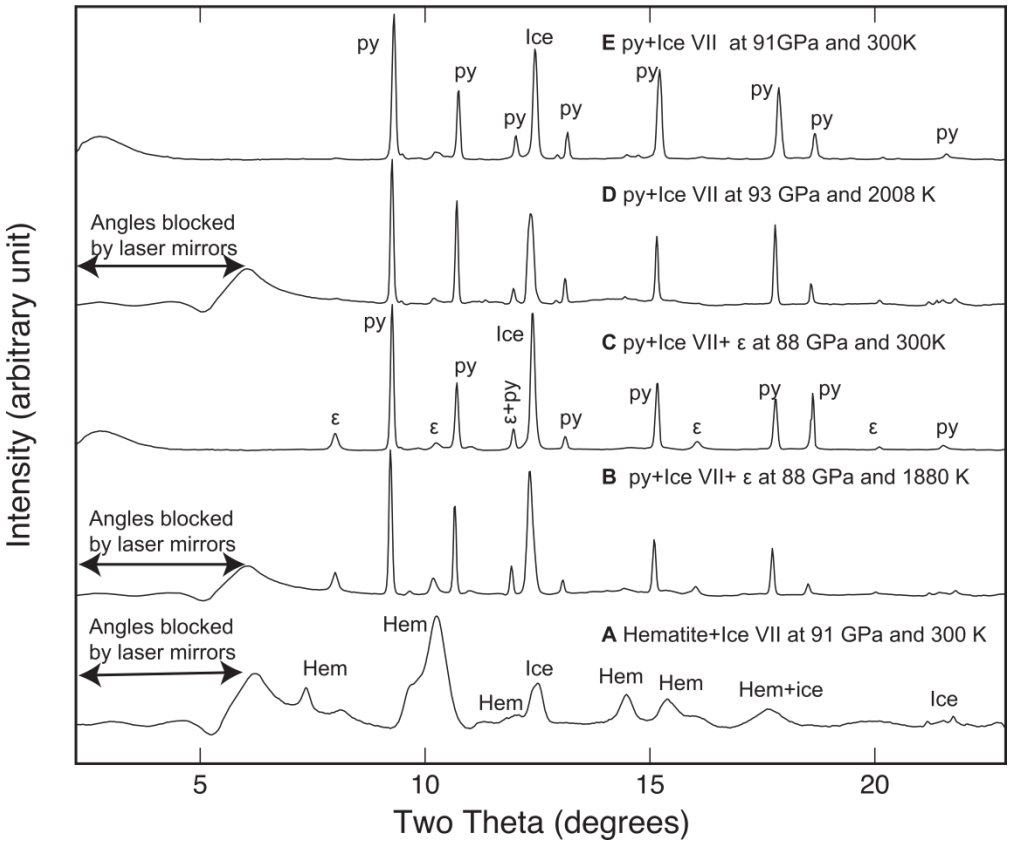

870

871

872 Fig S3. X-ray diffraction patterns for the py phase observed in this study: (A) an X-

873 ray diffraction pattern measured before laser heating at 91 GPa and 300 K, (B) a

874 pattern measured during laser heating at 88 GPa and 1880 K, (C) a pattern measured

875 after laser heating at 88 GPa and 300 K, (D) a pattern measured during laser heating

876 at 93 GPa and 2008 K, and (E) a pattern measured after laser heating at 91 GPa.

877

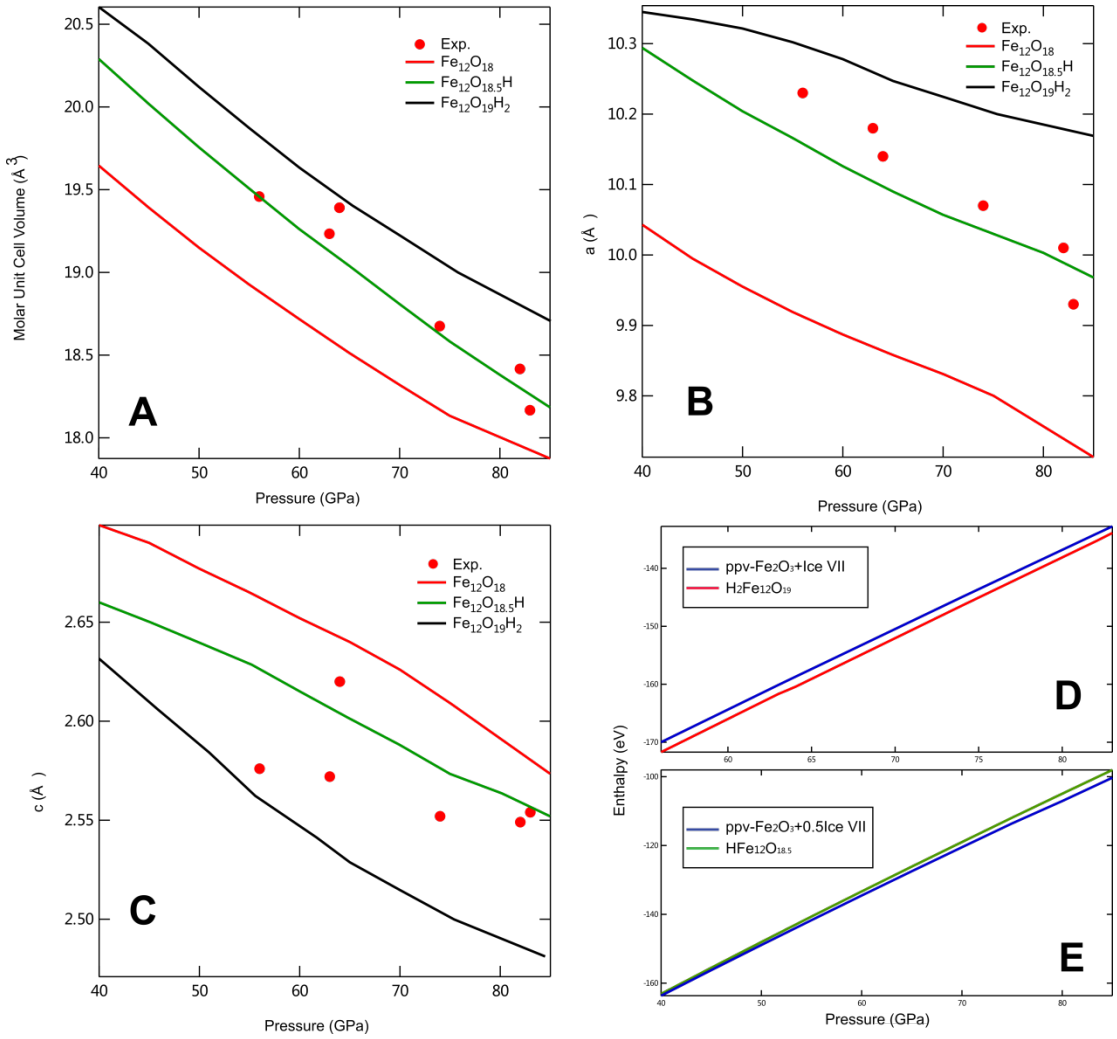

878

879 Fig. S4. The unit-cell volume and enthalpy of the η phase from our DFT calculations.

880 The parameters are compared with our experimental results (red circles). The red,

881 green, and black lines are for $Fe_{12}O_{18}$, $Fe_{12}O_{18.5}H$, and $Fe_{12}O_{19}H_2$, respectively, in (A),

882 (B) and (C). The enthalpies of these compositions were also compared in (D) and (E)

883 with ppv-Fe_2O_3 + Ice VII (blue).

884

885

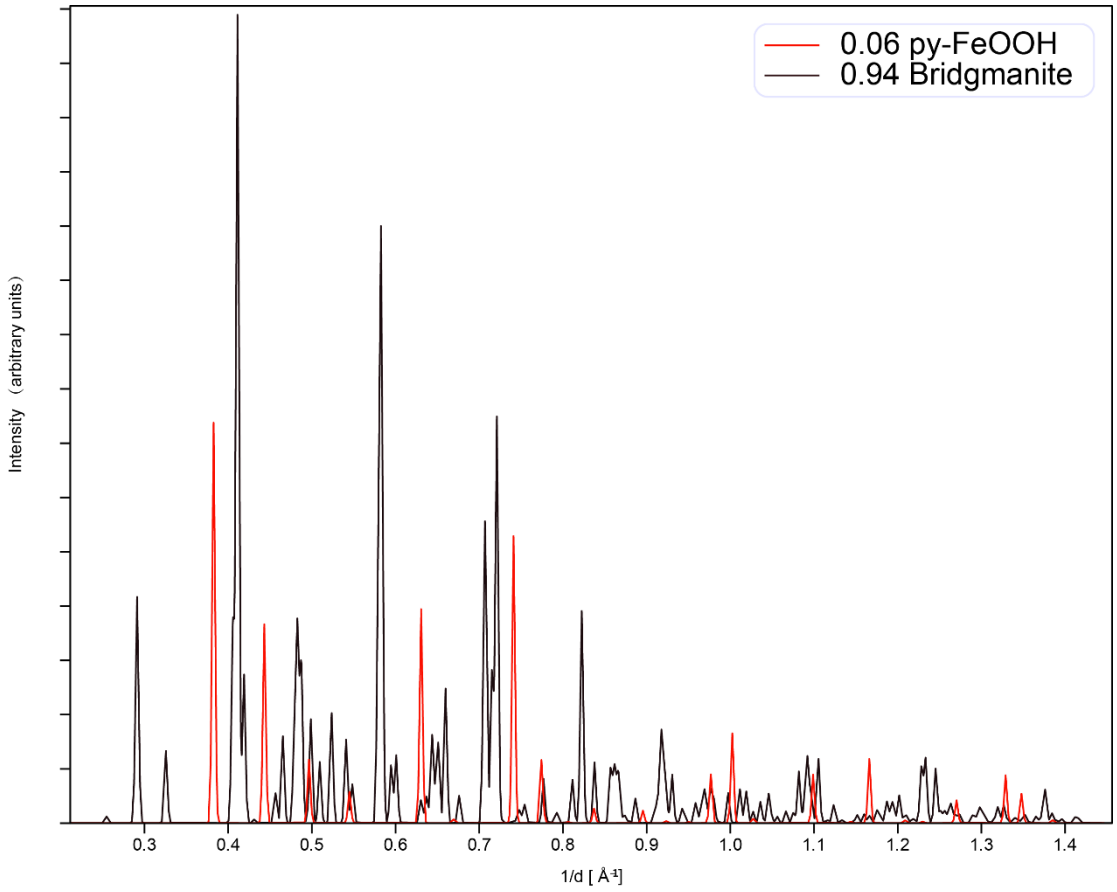

Fig. S5. A calculated diffraction pattern for 6 mol% py-FeOOH and 94 mol% bridgmanite. The unit-cell parameters of bridgmanite are from Ross and Hazen (1990). We used 86.4 $Å^3$ for the unit-cell volume of py-FeOOH.

References:

Altomare, A., Caliandro, R., Camalli, M., Cuocci, C., Giacovazzo, C., Moliterni, A.G., Rizzi, R., 2004. Automatic structure determination from powder data with EXPO2004. J Appl Crystallogr 37, 1025–1028.

Chen, H., Shim, S.-H., Leinenweber, K., Prakapenka, V., Meng, Y., Prescher, C., 2018. Crystal structure of $CaSiO_3$ perovskite at 28–62 GPa and 300 K under quasi-hydrostatic stress conditions. Am Miner. 103, 462–468.

Corma, A., Díaz-Cabañas, M., Jiang, J., Afeworki, M., Dorset, D., Soled, S., Strohmaier, K., 2010. Extra-large pore zeolite (ITQ-40) with the lowest framework density containing double four-and double three-rings. Proc Natl Acad Sci 107, 13997–14002.

Favre-Nicolin, V., Černỳ, R., 2002. FOX,free objects for crystallography': a modular approach to ab initio structure determination from powder diffraction. J Appl Crystallogr 35, 734–743.

Palatinus, L., Chapuis, G., 2007. SUPERFLIP–a computer program for the solution of crystal structures by charge flipping in arbitrary dimensions. J Appl Crystallogr 40, 786–790.

Putz, H., Schön, J., Jansen, M., 1999. Combined method for ab initio structure solution from powder diffraction data. J Appl Crystallogr 32, 864–870.

Ross, N.L., Hazen, R.M., 1990. High-pressure crystal chemistry of $MgSiO_3$ perovskite. Physics and Chemistry of Minerals 17, 228–237.